Nano Research

Open Access

Research Article

Decoupling nucleation and growth control for size-tunable spherical Ni nanoparticles and their tailored electrical and magnetic properties

Jie Zhu[1,3,4,§], Wenxin Zhan[2,§], Dawei Liu[2], Yongchang Zhang[2], Mingxiang Huang[5], Haiyan Zhao[4], Jianwei Wang[1,3] ✉, Yang Wu[5] ✉, and Junfeng Liu[2] ✉

[1] *GRINM NEXUSX Advanced Materials (Beijing) Co. Ltd., Beijing 101407, China*
[2] *State Key Laboratory of Chemical Resource Engineering, Beijing University of Chemical Technology, 15 Beisanhuan East Road, Chaoyang District, Beijing 100029, China*
[3] *China GRINM Group Co. Ltd., Beijing 100088, China*
[4] *Department of Mechanical Engineering, Tsinghua University, Beijing 100084, China*
[5] *College of Mathematics and Physics, Beijing University of Chemical Technology, Beijing 100029, China*
[§] *Jie Zhu and Wenxin Zhan contributed equally to this work.*

Cite this article: *Nano Research*, **2026**, *19*, 94908493. https://doi.org/10.26599/NR.2026.94908493

ABSTRACT: Miniaturizing electronic components calls for controlled synthesis of conductive metal nanoparticles with tunable and narrow size distributions. This has become increasingly essential, yet a significant challenge for the use as conductive inks or pastes in various applications, including multilayer ceramic capacitors, flexible electronics, and magnetofluids. In this work, we report the controllable synthesis of uniform spherical nickel nanoparticles via a mild aqueous-phase reduction strategy using triethanolamine (TEA) as a modulating agent. Through strategic control of both the dosage and the timing of TEA addition, we successfully decoupled nucleation and growth stages, enabling precise particle size regulation within the 95–270 nm range. Moreover, electrical conductivity tests on both pressed Ni pellets and printed ink lines confirmed the inherited metallic nature. The correlation between particle size and conductivity can be attributed to enhanced interparticle neck formation during sintering, which reduces electrical resistance. Both magnetic saturation (M_s) and remanent magnetization (M_r) are also positively related to particle size, while coercivity (H_c) shows a converse relationship, consistent with a size-dependent transition from surface-disordered to bulk-like multidomain magnetic behavior. This study not only provides an environmentally benign and scalable strategy for size-tunable Ni nanoparticle synthesis but also offers new promises for their integration in next-generation electronic and magnetic devices.

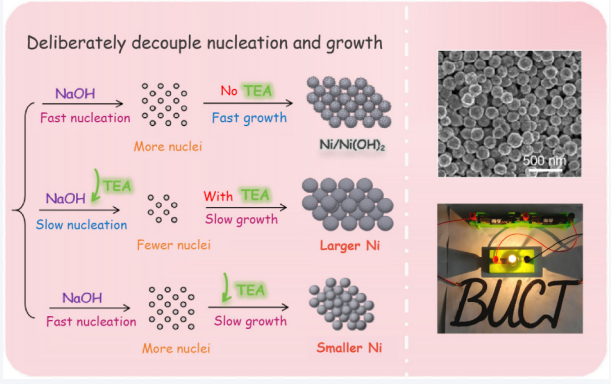

KEYWORDS: Ni nanoparticles, decoupled nucleation and growth, size-tunable synthesis, aqueous-phase reduction, electrical and magnetic properties

1 Introduction

Micron- and nano-sized nickel particles as a pivotal functional material have been widely applied in multilayer ceramic capacitors (MLCCs), chemical catalysis, energy storage, electric paste, and magnetic devices due to their high electrical conductivity, ferromagnetism, ductility, and corrosion resistance [1–6]. Current scaled production of nickel nanoparticles with high purity and crystallinity is dominated by physical or chemical vapor deposition techniques [7–9]. These approaches typically produce particles with broad size distributions ranging from tens of nanometers to several micrometers. However, the post-synthesis milling and isolation necessarily result in low production yields and high costs in complex equipment and energy consumption, limiting their scalability and economic viability. In contrast, the liquid-phase route is attracting growing attention as a more cost-effective and promising alternative that enables the synthesis of nickel

Received: December 27, 2025; **Revised:** January 22, 2026
Accepted: January 25, 2026

✉Address correspondence to Jianwei Wang, wangjianwei@grinm.com; Junfeng Liu, ljf@mail.buct.edu.cn; Yang Wu, wuy@buct.edu.cn

nanoparticles with precisely controllable size and morphology [10]. The critical part is the rational selection of stabilizing agents that regulate the nucleation and growth processes so as to finely tune the particle size and morphology to meet specific requirements [11–13]. For example, positively charged cations from cetyltrimethylammonium bromide (CTAB) adsorbing onto Ni particles can effectively improve nanoparticle dispersion and colloidal stability by generating repulsion during growth [14]. Trioctylphosphine (TOP) was employed as a capping agent, which selectively stabilized the crystal facets and suppressed isotropic growth of Ni particles, enabling the synthesis of monodisperse nanocubes via hydrogen-assisted reduction of $Ni(acac)_2$ [15]. However, stabilizing strategies that rely on strongly binding organic ligands realize effective morphological control at the expense of electrical and magnetic properties by surface passivation [16–18]. Moreover, these approaches are frequently conducted in organic solvents or under harsh reaction conditions, increasing process complexity and limiting scalability for practical applications [15, 19]. To warrant intrinsic properties of nanoparticles and their size-dependence, the balance between the prevention of severe surface oxidation and a high fraction of coverage by organic ligands is important for practical application. Therefore, there is an urgent need to develop mild and straightforward methods for the controlled synthesis of high-performance nickel nanoparticles.

Herein, we propose an all aqueous-phase synthetic method for spherical nickel nanoparticles with size tunability from 95 to 270 nm. By independently adjusting the dosage and adding timing of triethanolamine (TEA), we successfully decouple the nucleation and growth stages, thereby enabling more precise control over particle size. Particularly, we found the delayed TEA addition—introduced after the initial nucleation event—could suppress the subsequent growth process at no expense of initial nucleation, which leads to the formation of smaller nanoparticles. The synthesized Ni nanoparticles were further evaluated for their magnetic and electrical conductivity, both in pellet and ink-based forms, providing a comprehensive insight into the size-dependent functional properties relevant to electronic applications.

2 Results and discussion

2.1 Synthesis of spherical Ni nanoparticles

The synthesis of Ni nanoparticles was carried out in an aqueous alkaline solution at 65 °C using $NiCl_2·6H_2O$, $N_2H_4·H_2O$, and TEA as the nickel source, reductant, and capping agent, respectively (Fig. 1(a)). Typically, purple Ni-hydrazine complexes were first prepared by adding excessive $N_2H_4·H_2O$ to an aqueous solution of $NiCl_2·6H_2O$ (Fig. S1(a) in the Electronic Supplementary Material (ESM)). No significant precipitate was observed at this stage. Subsequently, an aqueous TEA solution with a molar ratio of $[TEA]/[Ni^{2+}] = 1$ was introduced, followed by the addition of a NaOH solution to adjust the pH to 13. The addition of the alkaline solution rapidly converted the purple Ni-hydrazine complex into bright green $Ni(OH)_2$ (Fig. S1(b) in the ESM). Moreover, the increased alkalinity significantly enhanced the reducing power of $N_2H_4·H_2O$, thereby accelerating the reduction process. After being stirred at 65 °C for 1 h, the suspension gradually turned black, resulting in the formation of Ni.

The scanning electron microscopy (SEM) was used to characterize the size and morphology of as-synthesized Ni nanoparticles. Figure 1(b) shows the overall morphologies of as-obtained products with low magnification, confirming that they were well dispersed and uniformly spherical. Statistical analysis revealed a Gaussian-like distribution of diameter with an average of 220 nm (Fig. 1(c)), and a size distribution from 175–275 nm (Fig. 1(d)). The as-prepared Ni nanoparticles were then verified with X-ray diffraction (XRD), where all distinguishable peaks

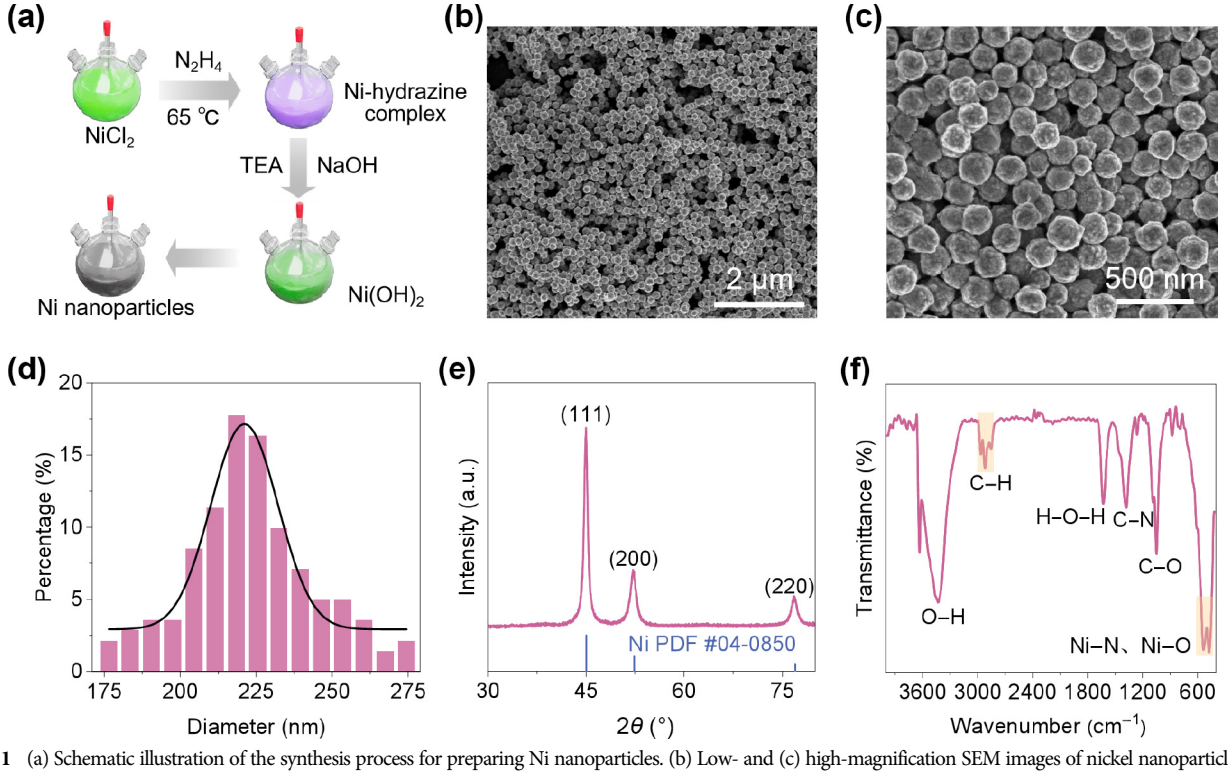

Figure 1 (a) Schematic illustration of the synthesis process for preparing Ni nanoparticles. (b) Low- and (c) high-magnification SEM images of nickel nanoparticles, and (d) along with the corresponding statistical histogram of particle size distribution and fitting. (e) XRD pattern and (f) FT-IR spectrum of Ni nanoparticles.

correspond to (111), (200), and (220) diffraction of Ni with space group $Fm\bar{3}m$ (JCPDS No. 04-0850) (Fig. 1(e)). High purity of the products was confirmed by the absence of impurity peaks.

The surface chemical states of the as-prepared Ni nanoparticles were analyzed using Fourier-transformed infrared spectroscopy (FT-IR) and X-ray photoelectron spectroscopy (XPS). The FT-IR spectrum (Fig. 1(f)) exhibits distinct vibrational bands associated with O-H (~ 3400 cm^{-1}), C–H (2850–2967 cm^{-1}), C–N (1377 cm^{-1}), and C–O (1047 cm^{-1}), resulting from the presence of TEA functional groups. Those in the 400–600 cm^{-1} region can be assigned to Ni–N and Ni–O stretching vibrations, implying the chemical interaction between TEA and Ni. These results are further supported by XPS analysis. The Ni 2p spectrum (Fig. S2 in the ESM) displays characteristic peaks corresponding to metallic Ni^0 as well as dominant Ni^{2+} species, likely originating from the surface coordination of nickel centers with TEA. Taken together, the FT-IR and XPS results indicate that TEA interacts with the Ni surface to stabilize the nanoparticles.

2.2 Particle size regulation by TEA

Since size is a well-known tuning knob for the intrinsic properties of nanomaterials, its precise control is of great importance for applications. According to the classical LaMer model, particle size is governed by the balance between nucleation and growth processes, where the reduction rate plays a key role. Rapid reduction rate tends to make a highly supersaturated reaction condition with accelerated accumulation and burst nucleation for smaller particle sizes [20]. On the other hand, a slower reduction rate decreases the concentration of the nucleus and hence leads to larger particles. To understand the growth mechanism and further elucidate the role of TEA in the liquid-phase reduction system, a series of control experiments with varying TEA/Ni^{2+} molar ratios was conducted. It is observed that higher TEA dosages consistently resulted in prolonged reduction time, defined as the time required for the reaction mixture to completely evolve from green $Ni(OH)_2$ to a uniform black suspension of Ni nanoparticles (Fig. 2(a) and Fig. S3 in the ESM). Specifically, the reduction time was approximately 15 min in the absence of TEA, while it increased to 20, 30, 60, 80,

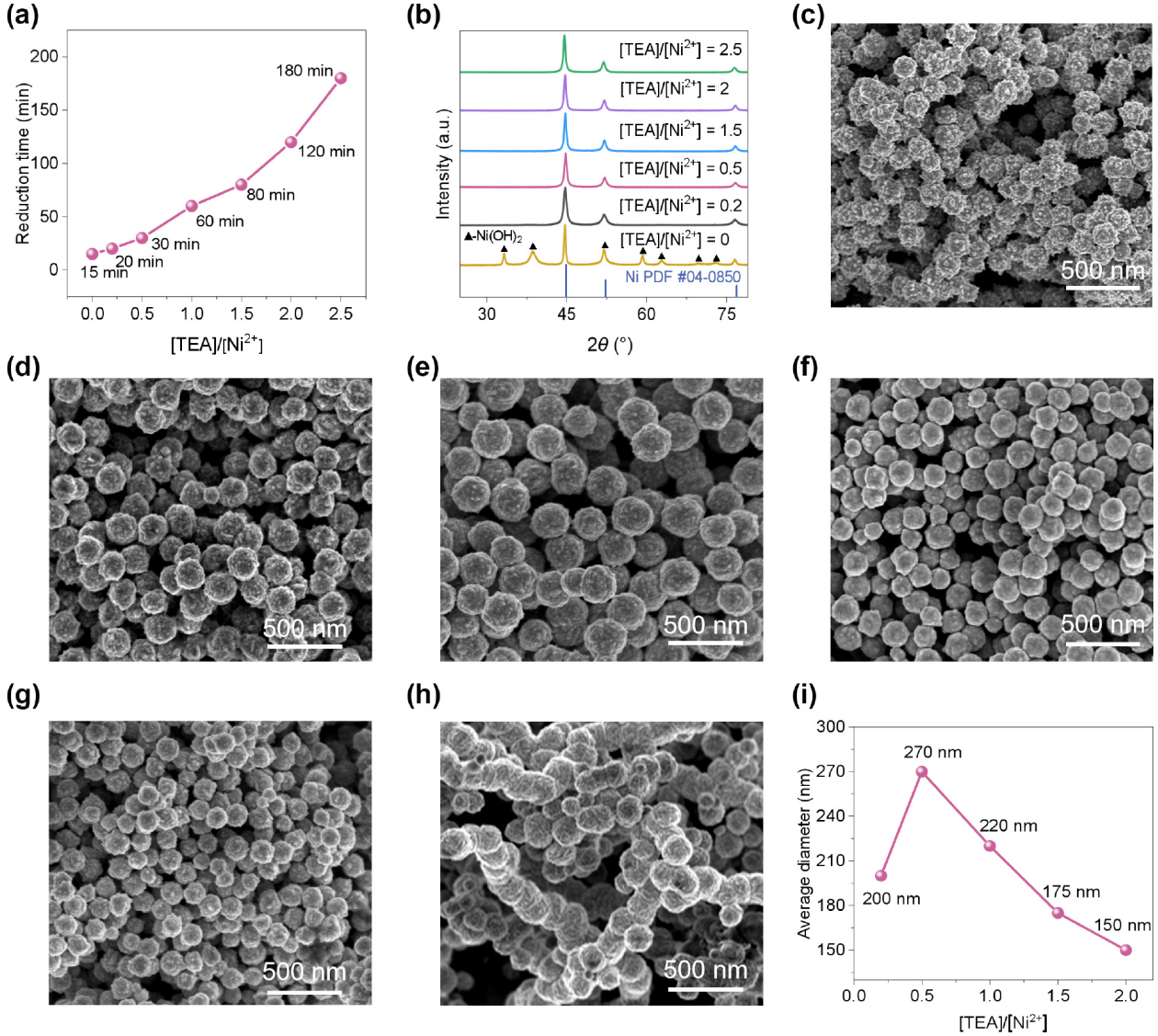

Figure 2 (a) Reduction time as a function of [TEA]/[Ni^{2+}] ratio. (b) XRD patterns of nickel nanoparticles obtained under different [TEA]/[Ni^{2+}] ratios. (c)–(h) SEM images of nickel nanoparticles synthesized with different molar ratios of [TEA]/[Ni^{2+}]: (c) 0, (d) 0.2, (e) 0.5, (f) 1.5, (g) 2.0, and (h) 2.5. (i) Variation of the average particle diameter as a function of [TEA]/[Ni^{2+}] ratio.

120, and 180 min upon the addition of TEA at TEA/Ni^{2+} molar ratios of 0.2, 0.5, 1, 1.5, 2, and 2.5, respectively. This trend reflects the coordinating effect of TEA, which significantly reduces the Ni^{2+} reduction rate, thereby suppressing both the nuclei and growth rate of Ni nanoparticles. XRD analysis confirmed the phase purity of the final products (Fig. 2(b)). Upon TEA addition, all final products consist exclusively of pure phase metallic Ni. However, in the absence of TEA, the $Ni(OH)_2$ phase is detected as impurity. SEM study further revealed a sea urchin-like morphology with an average size of 200 nm (Fig. 2(c)). To elucidate the role of TEA in stabilizing Ni nanoparticles against oxidation, a control experiment was conducted by introducing TEA after the formation of Ni nanoparticles under TEA-free condition. The resulting XRD pattern revealed the absence of $Ni(OH)_2$ phase (Fig. S5 in the ESM), demonstrating that $Ni(OH)_2$ observed in TEA-free samples originates from surface oxidation of freshly formed Ni^0 rather than incomplete reduction during synthesis. Additionally, $Ni(OH)_2$ intermediates formed following NaOH addition under both TEA-containing and TEA-free conditions were characterized via TEM, which exhibit similar sheet-like aggregated morphologies corresponding to $Ni(OH)_2$ phase (Fig. S4 in the ESM), suggesting that TEA does not alter the nature of the intermediate but primarily regulates the growth of Ni particles during subsequent nucleation.

Following the addition of TEA, the product exhibited isotropic growth with spherical morphology, resulting in a relatively smooth surface and better dispersion. Interestingly, the size distribution of the Ni particles exhibited a non-monotonic trend, initially increasing and then decreasing with increasing TEA/Ni^{2+} molar ratio. As shown in Figs. 2(d)–2(h), and Figs. S6 and S7 in the ESM, at low TEA concentrations ([TEA]/[Ni^{2+}] = 0.2–0.5), the average particle size increased from 190 to 270 nm, suggesting that a moderate amount of TEA retards the reduction process and reduces the effective nucleation density. When the concentration of TEA was further increased ([TEA]/[Ni^{2+}] = 0.5–2), the particle size decreased from 270 to 150 nm (Fig. 2(i)), indicating that enhanced surface passivation, which gradually suppressed particle growth, became dominant at higher TEA concentration. In summary, at lower concentrations, TEA may decrease the nucleation density to yield larger particles, but at higher concentrations, its surface capping effect may restrict particle growth and result in smaller sizes. As ratios exceeding 2, Ni nanoparticles spontaneously self-assembled into pearl-like chains, likely driven by weak but persistent and directional magnetic interactions between nascent Ni particles, which can be attributed to the significant retardation of the reduction process by excess TEA [21].

Accordingly, it can be deduced that TEA plays a dual role in modulating reaction kinetics in aqueous reduction systems, enabling control over particle size by reducing the effective nucleation rate of Ni species and directing spherical particle growth through surface capping. Therefore, to obtain smaller nanoparticles, we further propose and demonstrate a strategy involving the deliberate delay of TEA addition after the boosted nucleation process, thereby decoupling the nucleation and growth stages (Fig. 3). Taking the [TEA]/[Ni^{2+}] ratio of 1 as an example, simultaneous addition of TEA and NaOH produced particles with an average size of approximately 220 nm. However, if TEA addition was delayed until 30 s after NaOH introduction—at which time the solution had completely changed from purple to green, corresponding to full conversion of Ni species from hydrazine complexes into $Ni(OH)_2$—the average particle size decreased from

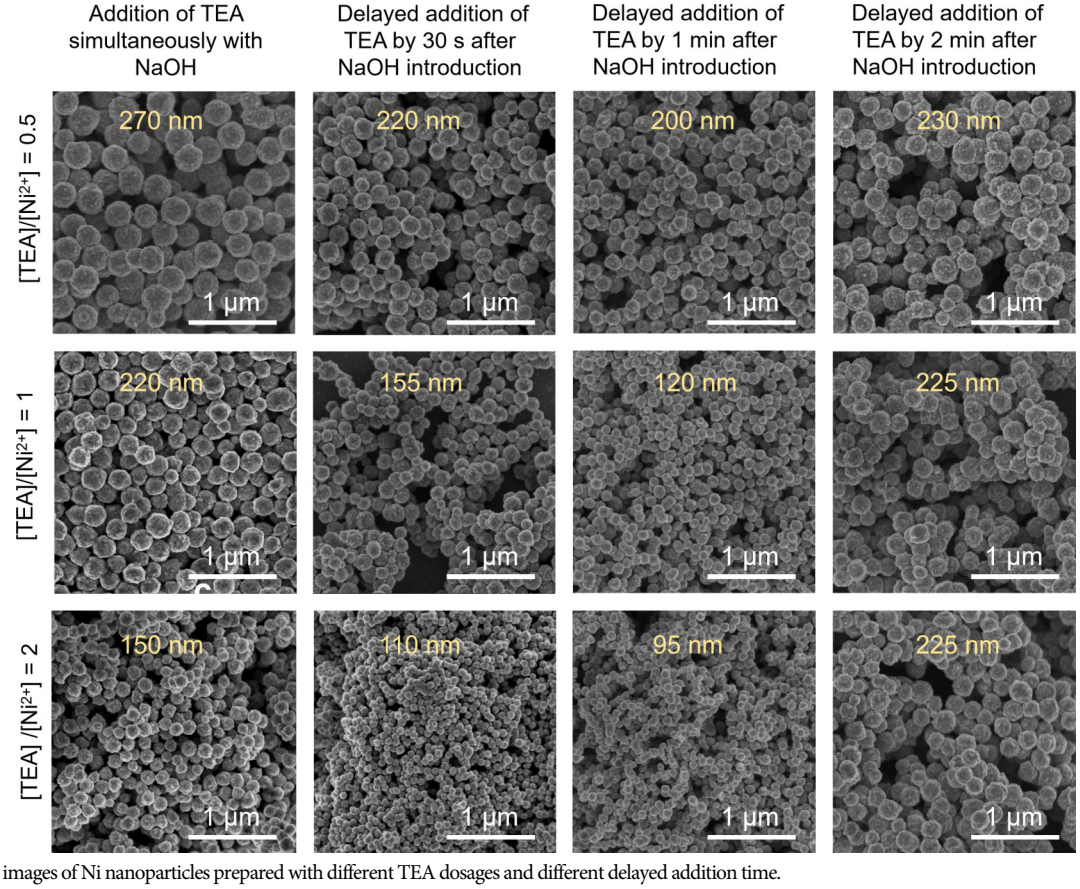

Figure 3 SEM images of Ni nanoparticles prepared with different TEA dosages and different delayed addition time.

220 to 155 nm. With a delay time of 1 min, during which the solution began to show a slightly darker hue due to the formation of a small amount of Ni^0, the system yielded the smallest particles with an average diameter of 120 nm. This pronounced size reduction demonstrates the effectiveness of delaying TEA addition in producing finer particles, and the underlying mechanism can be understood by the decoupling of nucleation and growth processes based on the LaMer model. As illustrated in Fig. 4, TEA is essential for obtaining a pure-phase Ni product, as it protects the nanoparticle surface from oxidation to $Ni(OH)_2$. However, the addition of TEA before the nucleation process significantly reduces the nucleation rate, resulting in fewer nuclei and consequently larger Ni nanoparticles in the final product.

In contrast, the delayed introduction of TEA after the nucleation stage allowed an initial burst of nucleation, leading to the formation of a high density of Ni nuclei. Subsequent capping by TEA restricted their further growth by inhibiting ion diffusionand crystal growth, thereby resulting in smaller, phase-pure Ni nanoparticles. In addition, when TEA was introduced at a further delay time of 2 min, the particle size increased again to approximately 225 nm, comparable to the case without TEA addition, but with a more regular and smoother surface, and improved phase purity. This observation indicates that nucleation was essentially completed within the first minute, and subsequent introduction of TEA just influenced the proceeding growth stage but was irrespective of the nucleation density. Thus, larger particles were observed. Similar trends were observed across other examined $[TEA]/[Ni^{2+}]$ ratios, such as 0.5 and 2.0. In particular, at $[TEA]/[Ni^{2+}] = 2$, delaying the TEA addition to 1 min yielded the smallest particles (~ 95 nm). These results indicate that the particle size is governed not only by the dosage of TEA, but more importantly by the timing of its addition, and highlight the importance of decoupling the nucleation and growth processes for controlling the size of Ni nanoparticles. In addition, to further evaluate the dispersibility and colloidal stability of the Ni nanoparticles, dynamic light scattering (DLS) and zeta potential measurements were performed on four representative Ni nanoparticle samples with average sizes of approximately 95, 120, 180, and 220 nm as determined by SEM. The corresponding hydrodynamic diameters measured by DLS were 103, 135, 201, and 230 nm, respectively (Fig. S7 in the ESM), and the zeta potential values ranged from 27.4 to 31.4 mV (Table S1 in the ESM), confirming good colloidal stability and dispersibility of the Ni nanoparticles in suspension. The slightly larger DLS sizes compared to those from SEM can be attributed to the presence of a solvation layer and weak interparticle interactions in aqueous dispersion.

2.3 Size-dependent electrical conductivity of nickel nanoparticles

The practical application of nickel nanoparticles in MLCCs, printed electronics, and electromagnetic shielding materials critically depends on their electrical conductivity [22, 23]. In this study, the electrical conductivity was evaluated via two representative forms of sample: hot-pressed pellets and ink-pasted strip lines, as shown in Figs. 5(a)–5(c) and Table 1. The pellets were prepared by hot-pressing at 600 °C under 50 MPa for 30 min, yielding discs with a diameter of 6 mm and a thickness of 0.8 mm. The relative densities of hot-pressed Ni pellets fabricated from Ni nanoparticles with varying sizes, as summarized in Table S2 in the ESM, range from 83.1%–89.4%, indicating effective densification during the hot-pressing process. As shown in Fig. 5(a) and Table 1, the electrical conductivity is positively related to particle size. Specifically, as the Ni particle size increased from 95 to 270 nm, the conductivity increased from 8.15 to 8.96 × 10^6 S/m, likely due to the reduced grain boundary scattering and improved inter-particle electrical pathway continuity in larger particles [24, 25]. Moreover, with the increasing demand for miniaturization of electronic devices, the required thickness of the conductive layer is correspondingly decreasing. Therefore, we further evaluate the electrical conductivity of hot-pressed pellets fabricated using, for instance, 95 nm Ni nanoparticles as a representative small-particle system, with pellet thickness decreased gradually to 100 and 10 μm. The conductivity slightly decreased from 8.05 × 10^6 S/m for pellets 100 μm-thick to 7.45 × 10^6 S/m for those 10 μm-thick (Fig. 5(b)). Importantly, even when the pellets were continuously thinned, the conductivity remains on the same order of magnitude as 0.8 mm pellets (8.15 × 10^6 S/m), verifying that the intrinsic electric property of the Ni nanoparticles is well preserved.

Nickel-based conductive inks were formulated by dispersing as-synthesized nanoparticles in glycerol with 50 wt.%. The ink was

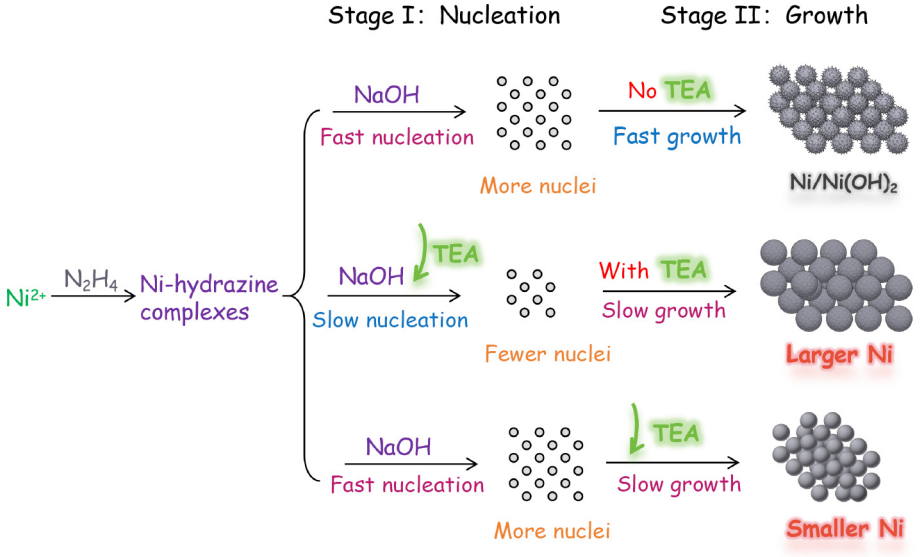

Figure 4 Schematic illustration of TEA-regulated nucleation and growth processes for spherical Ni nanoparticles.

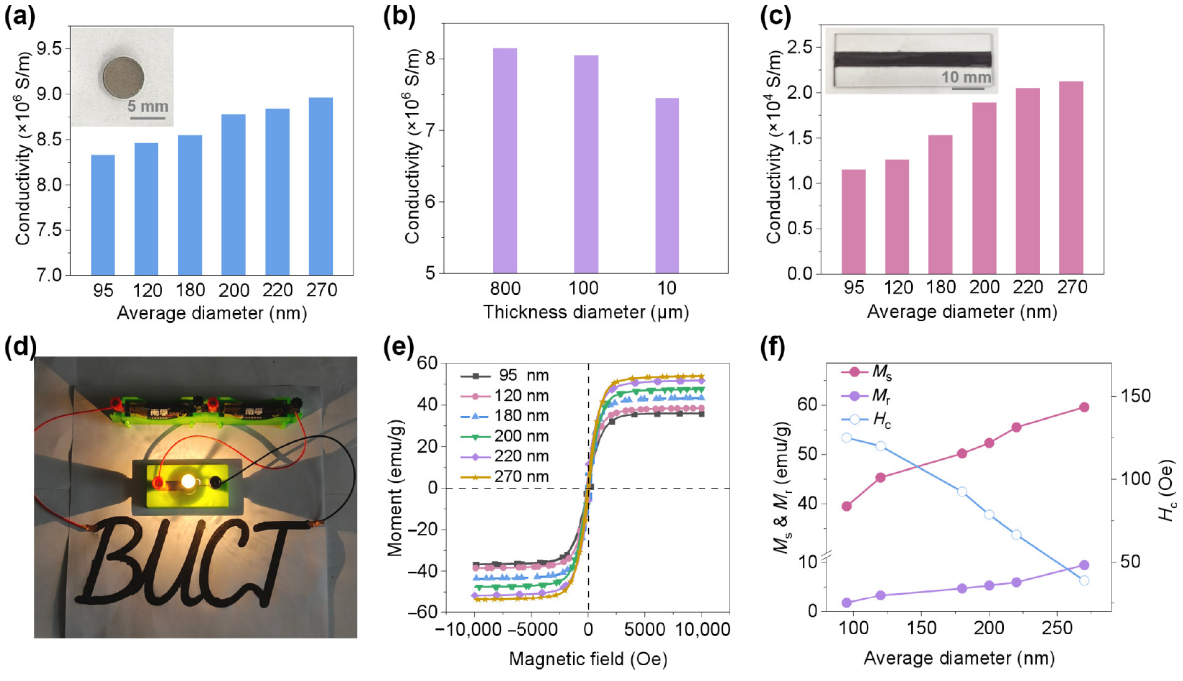

Figure 5 (a) Electrical conductivity of hot-pressed pellets as a function of average diameter of Ni particles. (b) Pellet thickness-dependence of electrical conductivity for 95 nm Ni. (c) Electrical conductivity as a function of average diameter of ink-based strip lines. (d) Paper-based "BUCT" circuit drawn with 270 nm Ni ink, showing a single LED powered at 3 V. (e) Room temperature M-H loops of Ni nanoparticles of different sizes. (f) Effect of particle size on the M_s and M_r (left axis), and H_c (right axis) of Ni nanoparticles.

Table 1 Electrical and magnetic properties of nickel nanoparticles with different sizes

Average particle size (nm)	Electrical conductivity		Magnetic properties		
	Pellet (S/m)	Ink (S/m)	M_s (emu/g)	M_r (emu/g)	H_c (Oe)
95	8.15×10^6	1.15×10^4	35.9	1.73	125
120	8.29×10^6	1.26×10^4	38.5	3.97	120
180	8.51×10^6	1.53×10^4	43.4	4.73	92.5
200	8.77×10^6	1.89×10^4	47.6	5.34	78.7
220	8.84×10^6	2.05×10^4	51.5	6.01	66.5
270	8.96×10^6	2.12×10^4	53.9	9.48	38.9

blade-coated onto glass substrates, with the coating area defined using triple-layered tape masks. After drying, the films were heated at 600 °C for 30 min under an argon atmosphere to remove the organic solvent and promote particle sintering. The resulting conductive strips had dimensions of approximately 5 mm × 50 mm × 0.5 mm (Fig. 5(c) inset). The sintered ink lines also showed a positive particle size-dependent conductivity, consistent with the pellet samples (Fig. 5(c)). In comparison, the conductivity of ink lines was lower than that of the pellets, likely due to lower packing density and residual organics, which introduced additional contact resistance [26–28]. Notably, both measurements converged that larger nickel particles yield higher electrical conductivity. To further demonstrate the practical applicability of the nickel-based conductive ink, a proof-of-concept circuit was fabricated using the 270 nm Ni nanoparticle ink, which exhibited the highest conductivity. As shown in Fig. 5(d), a conductive writing of "BUCT" was painted on standard A4 paper using a commercial pen filled with the Ni ink. After drying at 80 °C overnight, the proof-of-concept circuit stably lit up an LED under a driving DC voltage of 3 V. These results render such nickel ink decent functional electrical pastes for printable circuits on a variety of substrates via simple, low-temperature processes, highlighting their potential for applications in MLCC electrodes, wearable and flexible electronics.

2.4 Size-dependent magnetism of nickel nanoparticles

Magnetic properties are crucial parameters that determine the applicability of nickel nanoparticles in information storage devices, electromagnetic shielding, and magnetofluids [29]. To clarify the correlation between particle size and magnetic behavior, a series of magnetic measurements was conducted on various nickel nanoparticles. The results are presented in Figs. 5(e) and 5(f), and Fig. S8 in the ESM, and summarized in Table 1. Ni nanoparticles show a size-dependent superparamagnetism. As particle size increased, saturation magnetization (M_s) and remanent magnetization (M_r) exhibited a progressive increase, while coercivity (H_c) showed a contrary trend. The enhancement in M_s and M_r with increasing size is attributed to the reduction of surface spin disorder and the increased contribution of bulk-like magnetic moments [30]. Meanwhile, the observed decrease in H_c with increasing particle size is correlated with the multidomain structure of Ni nanoparticles. Specifically, larger particles facilitate the domain-wall motion, thereby reducing the energy barrier required for magnetization reversal [31, 32].

3 Conclusion

In conclusion, we developed an innovative aqueous strategy for the controlled synthesis of uniform spherical nickel nanoparticles. By systematically varying both the dosage and addition timing of TEA, we achieved fine regulation over reduction kinetics, nucleation density, and growth dynamics by decoupling the nucleation and growth stages. This strategy afforded a promising approach in aqueous Ni synthesis and allowed for versatility in particle size

tuning from 270 nm down to 95 nm. Moreover, both pellet- and ink-based electrical tests confirmed superior conductivity. Magnetic measurements revealed a superparamagnetic behavior. This work not only offers new mechanistic insights into TEA-regulated hydrazine-based Ni nanoparticle formation but also provides a scalable, tunable, and low-temperature synthetic route for Ni nanoparticles, paving the way for future applications in MLCC electrodes, printed conductors, and magnetic devices.

Electronic Supplementary Material: Supplementary Material (experimental details, material characterization, electrical conductivity, and magnetic properties measurements) is available in the online version of this article at https://doi.org/10.26599/NR.2026.94908493.

Data availability

All data needed to support the conclusions in the paper are presented in the manuscript and the Electronic Supplementary Material. Additional data related to this paper may be requested from the corresponding author upon request.

Acknowledgements

This work was financially supported by the Beijing Natural Science Foundation (No. L245003), the National Natural Science Foundation of China (No. 92365204), Open Research Program of State Key Laboratory of Enhanced Oil & Gas Recovery (No. 5KTKFSC091), and Fundamental Research Funds for the Central Universities (No. buctrc202212).

Declaration of competing interest

The authors declare that they have no known competing financial interests or personal relationships that could have appeared to influence the work reported in this paper.

Author contribution statement

J. Z.: Conceptualization, funding acquisition, writing – review & editing. W. X. Z.: Methodology, formal analysis, experimental analysis, data curation. D. W. L.: Investigation, writing – original draft. Y. C. Z.: Data curation. M. X. H.: Data curation. H. Y. Z.: Supervision. J. W. W.: Conceptualization. Y. W.: Methodology, supervision, writing – review & editing. J. F. L.: Conceptualization, writing – review & editing, project administration, funding acquisition.

Use of AI statement

None.

References

[1] Goesmann, H.; Feldmann, C. Nanoparticulate functional materials. *Angew. Chem., Int. Ed.* **2010**, *49*, 1362–1395.

[2] e Silva, F. A.; Salim, V. M. M.; Rodrigues, T. S. Controlled nickel nanoparticles: A review on how parameters of synthesis can modulate their features and properties. *AppliedChem* **2024**, *4*, 86–106.

[3] Jaji, N. D.; Lee, H. L.; Hussin, M. H.; Akil, H. M.; Zakaria, M. R.; Othman, M. B. H. Advanced nickel nanoparticles technology: From synthesis to applications. *Nanotechnol. Rev.* **2020**, *9*, 1456–1480.

[4] Hong, K.; Lee, T. H.; Suh, J. M.; Yoon, S. H.; Jang, H. W. Perspectives and challenges in multilayer ceramic capacitors for next generation electronics. *J. Mater. Chem. C* **2019**, *7*, 9782–9802.

[5] Feng, P. X.; Chen, Q. L.; Yang, D. J.; Wang, H. Nitrogen-doped lignin mesoporous carbon/nickel/oxide nanocomposites with excellent lithium storage properties. *Rare Met.* **2025**, *44*, 889–900.

[6] Li, Z.; Chen, Z. B.; Ji, X. D.; Jin, H. H.; Si, Y. F.; Zhang, J. W.; Chen, C.; He, D. P. Controlling electrodeposited Ni layers by different-sized graphene oxides enables conductive e-textiles for the highly sensitive electrochemical detection of glucose. *Nano Res.* **2024**, *17*, 6258–6264.

[7] Jo, Y. S.; Lee, H. J.; Park, H. M.; Na, T. W.; Jung, J. S.; Min, S. H.; Kim, Y. K.; Yang, S. M. Chemical vapor synthesis of nonagglomerated nickel nanoparticles by in-flight coating. *ACS Omega* **2021**, *6*, 27842–27850.

[8] Escorcia-Díaz, D.; García-Mora, S.; Rendón-Castrillón, L.; Ramírez-Carmona, M.; Ocampo-López, C. Advancements in nanoparticle deposition techniques for diverse substrates: A review. *Nanomaterials* **2023**, *13*, 2586.

[9] Cushing, B. L.; Kolesnichenko, V. L.; O'Connor, C. J. Recent advances in the liquid-phase syntheses of inorganic nanoparticles. *Chem. Rev.* **2004**, *104*, 3893–3946.

[10] Wu, Z. G.; Munoz, M.; Montero, O. The synthesis of nickel nanoparticles by hydrazine reduction. *Adv. Powder Technol.* **2010**, *21*, 165–168.

[11] Chen, X. W.; Alijani, S.; Gallarati, S.; Tessore, F.; Jose Delgado, J.; Gianolio, D.; Villa, A.; Arrigo, R. Investigation on the structure and performance of supported Ni nanoparticles for the hydrogenation of furfural. *ChemCatChem* **2024**, *16*, e202400229.

[12] Ahghari, M. R.; Soltaninejad, V.; Maleki, A. Synthesis of nickel nanoparticles by a green and convenient method as a magnetic mirror with antibacterial activities. *Sci. Rep.* **2020**, *10*, 12627.

[13] Wan, K. L.; Zhang, T. Y.; Wang, H. J.; Liu, S.; Xie, C. B.; Gao, R. L.; Qin, Y. X.; Yang, X.; Guo, Y.; Wang, L. Y. et al. Encapsulation of Ni nanoparticles in O-doped carbon as chainmail electrocatalyst for alkaline seawater hydrogen evolution. *Innovation Mater.* **2025**, *3*, 100148.

[14] Chen, D. H.; Hsieh, C. H. Synthesis of nickel nanoparticles in aqueous cationic surfactant solutions. *J. Mater. Chem.* **2002**, *12*, 2412–2415.

[15] LaGrow, A. P.; Ingham, B.; Cheong, S.; Williams, G. V. M.; Dotzler, C.; Toney, M. F.; Jefferson, D. A.; Corbos, E. C.; Bishop, P. T.; Cookson, J. et al. Synthesis, alignment, and magnetic properties of monodisperse nickel nanocubes. *J. Am. Chem. Soc.* **2012**, *134*, 855–858.

[16] Walker, S. B.; Lewis, J. A. Reactive silver inks for patterning high-conductivity features at mild temperatures. *J. Am. Chem. Soc.* **2012**, *134*, 1419–1421.

[17] Jeong, S.; Song, H. C.; Lee, W. W.; Lee, S. S.; Choi, Y.; Son, W.; Kim, E. D.; Paik, C. H.; Oh, S. H.; Ryu, B. H. Stable aqueous based Cu nanoparticle ink for printing well-defined highly conductive features on a plastic substrate. *Langmuir* **2011**, *27*, 3144–3149.

[18] Ntallis, N.; Trohidou, K. N. Effect of organic coating variation on the electric and magnetic behavior of ferrite nanoparticles. *ACS Phys. Chem. Au* **2023**, *3*, 532–539.

[19] Heuer-Jungemann, A.; Feliu, N.; Bakaimi, I.; Hamaly, M.; Alkilany, A.; Chakraborty, I.; Masood, A.; Casula, M. F.; Kostopoulou, A.; Oh, E. et al. The role of ligands in the chemical synthesis and applications of inorganic nanoparticles. *Chem. Rev.* **2019**, *119*, 4819–4880.

[20] Lin, H. X.; Lei, Z. C.; Jian, Z. Y.; Hou, C. P.; Liu, D. Y.; Xu, M. M.; Tian, Z. Q.; Xie, Z. X. Supersaturation-dependent surface structure evolution: From ionic, molecular to metallic micro/nanocrystals. *J. Am. Chem. Soc.* **2013**, *135*, 9311–9314.

[21] Wilson, R. J.; Hu, W.; Fu, C. W. P.; Koh, A. L.; Gaster, R. S.; Earhart, C. M.; Fu, A. H.; Heilshorn, S. C.; Sinclair, R.; Wang, S. X. Formation and properties of magnetic chains for 100 nm nanoparticles used in separations of molecules and cells. *J. Magn. Magn. Mater.* **2009**, *321*, 1452–1458.

[22] Xu, X. F.; Dang, R.; Liu, J.; Li, M. X. Synthesis of Ni nanosheets by template-free method and their application in conductive and magnetic flexible electrons. *ACS Appl. Mater. Interfaces* **2023**, *15*, 36698–36705.
[23] Zhang, P.; Sun, Q. H.; Fang, S. Y.; Guo, H.; Liu, K.; Zhang, L. F.; Zhu, Q.; Wang, M. Fabrication of nano copper highly conductive and flexible printed electronics by direct ink writing. *ACS Appl. Mater. Interfaces* **2025**, *17*, 1847–1860.
[24] Montes, J. M.; Cuevas, F. G.; Cintas, J.; Gallardo, J. M. Electrical conductivity of metal powder aggregates and sintered compacts. *J. Mater. Sci.* **2016**, *51*, 822–835.
[25] Hajlaoui, M. E.; Dhahri, E.; Khirouni, K. High resistance and giant permittivity study of $Ni_{0.4}Zn_{0.6}Fe_2O_4$ spinel ferrite as a function of frequency and temperature. *J. Mater. Sci.: Mater. Electron.* **2022**, *33*, 18858–18870.
[26] Corrales‐Pérez, B.; Díaz‐Ufano, C.; Salvador, M.; Santana-Otero, A.; Veintemillas-Verdaguer, S.; Beni, V.; Morales, M. D. P. Alternative metallic fillers for the preparation of conductive nanoinks for sustainable electronics. *Adv. Funct. Mater.* **2024**, *34*, 2405326.
[27] McKibben, N.; Curtis, M.; Maryon, O.; Sawyer, M.; Lazouskaya, M.; Eixenberger, J.; Deng, Z. X.; Estrada, D. Formulation and aerosol jet printing of nickel nanoparticle ink for high-temperature microelectronic applications and patterned graphene growth. *ACS Appl. Electron. Mater.* **2024**, *6*, 748–760.
[28] Aeby, X.; Yan, X. M.; Huber, T.; Schneider, A.; Siqueira, G.; Nyström, G. 3D printing of highly electrically conductive zinc for sustainable electronics applications. *Adv. Mater. Technol.* **2025**, *10*, 2401132.
[29] Fantechi, E.; Innocenti, C.; Bertoni, G.; Sangregorio, C.; Pineider, F. Modulation of the magnetic properties of gold-spinel ferrite heterostructured nanocrystals. *Nano Res.* **2020**, *13*, 785–794.
[30] Vestal, C. R.; Zhang, Z. J. Effects of surface coordination chemistry on the magnetic properties of $MnFe_2O_4$ spinel ferrite nanoparticles. *J. Am. Chem. Soc.* **2003**, *125*, 9828–9833.
[31] Shafi, K. V. P. M.; Gedanken, A.; Prozorov, R.; Balogh, J. Sonochemical preparation and size-dependent properties of nanostructured $CoFe_2O_4$ particles. *Chem. Mater.* **1998**, *10*, 3445–3450.
[32] Mathew, D. S.; Juang, R. S. An overview of the structure and magnetism of spinel ferrite nanoparticles and their synthesis in microemulsions. *Chem. Eng. J.* **2007**, *129*, 51–65.